Seismic Dispersion and Attenuation in Fractured Fluid-Saturated Porous Rocks: An Experimental Study with an Analytic and Computational Comparison

Ariel Gallagher, Jérôme Fortin, Jan Borgomano

Seismic Dispersion and Attenuation in Fractured Fluid-Saturated Porous Rocks: An Experimental Study with an Analytic and Computational Comparison

Ariel Gallagher[1] · **Jérôme Fortin**[1] · **Jan Borgomano**[1,2]

Received: 1 September 2021 / Accepted: 31 March 2022

Abstract

Although different fluid pressure diffusion mechanisms caused by fractures have been extensively studied using analytical and numerical methods, there is little to no experimental work completed on them in laboratory conditions. In this paper, hydrostatic-stress oscillations (frequency – 0.04 to 1 Hz) are used on an intact and saw cut sample, in dry and water saturated conditions, in a triaxial cell at different effective pressures in undrained conditions. The objective is to study the fracture's effect on the elastic properties of the sample and validate some computational fracture models, that have been explored in the literature. Experimental results highlight dispersion and attenuation in saturated conditions due to the fracture, which diminishes in amplitude as the effective pressure is increased, i.e. as the fracture is closed. From local strain gauge measurements, it is found that there is a local negative phase shift between stress and strain in water saturated conditions for the fractured sample, due to the location of the strain measurements. No attenuation observed in dry conditions. A simple 1D model using mass balance and mechanical equilibrium equations for a linear isotropic poroelastic homogeneous medium give prediction in very good agreement with the experimental results. A 3D model was also developed to allow a comparison between analytic, numerical and experimental results.

Highlights

- Using innovative microvalves in an experimental setup on a fractured rock sample, to reach undrained conditions, in seismic frequency range.
- Local strain measurements, for the first time experimentally, show local negative phase shift between stress and strain in water saturated conditions.
- A 1D analytical and 3D numerical model were created which are in good agreement with the experimental results.

Keywords Rock mechanics · Experimental · Fracture · Attenuation

1 Introduction

Fractures are commonplace in reservoirs. Natural fractures are the consequence of geologic processes (cycle of burial, diagenesis, uplift, tectonic, erosional unloading…) but may also be created due to anthropogenic activities such as geothermal exploitation (Fleuchaus and Blum 2017). Even if they only account for a small amount of the total porosity of a geological formation, they may control the reservoir permeability (Walsh 1981; Paillet et al. 1987) and elastic properties (Matonti et al. 2015; Bailly et al. 2019); thus, a better knowledge of the effect of fractures on the physical properties of a reservoir is fundamental for deep geological repositories (Min et al. 2013), the exploitation of hydrocarbons (Gudmundsson and Løtveit 2014), CO_2 sequestration (Mazumder et al. 2006; Ulven et al. 2014) and geothermal exploitation.

✉ Ariel Gallagher
ariel.c.g.gallagher@gmail.com

[1] Laboratoire de Géologie, École Normale Supérieure, 24 Rue Lhomond, 75005 Paris, France

[2] MODIS, 4 Rue Jules Ferry, 64000 Pau, France

Fractures can be defined as a type of porosity with small aspect ratios which is more compliant than equant pores and as such is more sensitive to stress. As a consequence, elastic properties and thus P- and S- wave velocities are strongly affected by the fracture density, orientation, connectivity and geometry (Walsh 1981; Brajanovski et al. 2005; Gurevich et al. 2009; Galvin and Gurevich 2009, 2015; Quintal et al. 2014; Guo et al. 2018a, b; Lissa et al. 2020). The elastic wave velocities for fluid-saturated rocks, in the absence of mesoscopic (cm scale) fractures, can be frequency dependent resulting in attenuation and dispersion. This behavior has been shown to be attributed to different mechanisms. One of these fluid pressure diffusion (FPD) mechanisms is at a mesoscopic scale, between different regions and is dependent on the change in properties, such as compressibility, permeability and pore fluid viscosity, between regions (Müller et al. 2010). Heterogeneous rocks and multiple pore fluids can also create volumes of different compressibility which may trigger a similar viscoelastic response (White 1975). Squirt flow is another FPD mechanism which happens at pore scale, within the representative elementary volume (REV), between stiff and more compliant pores (Batzle et al. 2006; Gurevich et al. 2010). The characteristic frequency is related to the aspect ratio of the different microscopic pores, the elastic properties of the sample and is inversely proportional to the dynamic viscosity of the pore fluid.

In saturated condition, the presence of mesoscopic fractures can also change the elastic properties of samples by promoting dissipation through FPD. This has been shown through analytical modelling (Brajanovski et al. 2005; Gurevich et al. 2009; Galvin and Gurevich 2009, 2015), and also through numerical modelling with simple cases of a single fracture and simple stress fields applied (Chapman and Quintal 2018; Caspari et al. 2019), to slightly more complicated geometries of fractures intersecting each other at 90° (Vinci et al. 2014; Lissa et al. 2020), to even more complex geometries, such as multiple parallel fractures (Cai and Zhao 2000; Carcione et al. 2012) or even fractures intersecting at 45° (Quintal et al. 2014). Some work has also been done in situ at the Grimsel Test Site in the Swiss alps by Barbosa et al. (2019), who investigated the effect of fractures in a borehole, using a sonic logging tool, which allowed for P and S wave velocities as well as their attenuation measurements, with intrinsic background attenuation estimated and removed by studying the intact regions of the borehole.

However, there is a lack of data that investigates in the laboratory, under pressure and in undrained conditions, the frequency dependence of fractured porous rocks. Nakagawa (2013) was able to measure normal and shear fracture attenuation at a range of seismic frequencies (between 1 and 100 Hz) with different axial stresses applied normal to the fracture. This setup was not in a pressure vessel, therefore, limiting the stress oscillations to be purely axial and limiting the tests to have a very low pore pressure in the sample to prevent fluid migration between the jacket and the sample. Amalokwu et al. (2014) showed results on man-made intact sandstones and sandstones with aligned penny-shaped voids at different water saturation levels at 40 MPa effective pressure and measurements made at a single frequency of 650 kHz, which showed more attenuation in the sandstone with aligned penny-shaped voids. Amalokwu et al. note, however, that there can be microstructural differences between the intact and fractured samples due to manufacturing processes, which makes it hard to compare absolute attenuation peaks between both samples.

One needs to be careful regarding the definition of a local and global measurement, in a laboratory setting, when an isotropic medium has a fracture introduced to the sample. As a matter of fact, Chapman and Quintal (2018) investigated numerically the mechanical properties of a fully saturated Berea sandstone sample with a single fracture and distinguished (1) the elastic modulus of the whole fractured sample from (2) the apparent elastic modulus of the matrix (local measurement), both affected by the pore pressure variation induced by the fracture. In the second case, the results showed different attenuation peaks depending on where the local strain was measured (more or less close to the fracture). They also show that in this case, a negative phase shift between stress and strain is expected.

Finally, one needs to be especially careful that the measured attenuation is related to the fracture and not to other mechanisms like squirt-flow (Gurevich et al. 2010; Chapman and Quintal 2018), partial saturation (Chapman et al. 2016; Spencer and Shine 2016; Chapman et al. 2019), drained–undrained transition (Pimienta et al. 2016) or even mesoscopic FPD (Carcione and Picotti 2006).

The goal of this work is to validate numerical models by experimentally showing FPD caused by fractures, such as the simulation by Chapman and Quintal (2018). To accomplish this, the elastic properties of an intact sample were monitored during hydrostatic oscillations at a frequency range of 0.04–1 Hz in dry and water saturated conditions, with undrained boundaries, and at three effective pressures. The effective pressure is defined as the difference between the confining and pore pressure, with the confining and pore pressure defined as the pressure in the triaxial cell and the pressure in the pore fluid of the sample, respectively. The sample was then cut in half, to create a simple known fracture geometry. The fractured sample was then tested again following the same procedure as for the intact sample. Although, the fracture strain cannot be directly measured due to the experimental limitations, we measured the strain in the matrix—affected by pore pressure change due to the fracture—similar to what was investigated in Chapman and Quintal's work (2018), allowing comparisons to numerical

models in the literature. Permeability tests were completed on the intact and saw cut sample at varying effective pressures to estimate the hydraulic aperture and stiffness of the fracture in undrained conditions, using innovative microvalves. A 1D model was developed, using the hydraulic aperture and stiffness measured. The model is used to calculate the pore pressure field with frequencies as well as the bulk modulus and attenuation with frequency. In addition, a numerical model was made in COMSOL multiphysics to take into account the 3D geometry and validate the 1D model. Finally, the numerical and analytical models were compared to the experimental data.

2 Experimental Procedure

The dispersion and attenuation of the bulk modulus was measured using the stress–strain method (Adelinet al. 2011; David et al. 2013; Pimienta et al. 2015), in a TOP Industries™ triaxial cell (Fig. 1) installed at the ENS Paris geology laboratory (Borgomano et al. 2020). It is outfitted with three pumps, two of which are oil filled and control cell pressure and the axial piston, and the final pump is a Quizix dual pump (QX1500HC model), which is water filled and controls upstream and downstream pore pressures in the sample.

Four strain gauge pairs are attached to the surface of the sample at mid-height (Fig. 2) and are used to measure local strain during the hydrostatic-stress oscillations. The strain gauge pairs are two directional and have one axial and one radial component at 90° from each other. They have a resistance of 350 Ω and have a gauge length of 5 mm. The sample is held between a top and bottom cap, and is separated from the confining oil by a black neoprene jacket.

The strain gauges and the pressure transducers are connected to the data acquisition system (DAQ), which can record up to a frequency of 4 kHz. The cell pump controls the cell pressure and can reach a maximum pressure of 100 MPa with a hydrostatic oscillating mean amplitude of 0.2 MPa and a minimum and maximum oscillating frequency of 0.001 and 1.3 Hz, respectively.

It is important to underline that every test completed under pore fluid saturation in this paper was done in undrained conditions. This was accomplished using microvalves which are placed in the bottom and top end platen, which when closed reduce the dead volume to ~ 20 µl. The dead volume can be defined experimentally as the volume of fluid between the inlet and outlet of the sample and the pump or as an excess of water which acts as a fluid reservoir outside of the sample. This implies that the mass of fluid inside the sample during the oscillation is constant, a necessary condition to measure directly the undrained moduli (Fortin and Guéguen 2021). More details of the experimental set up regarding these microvalves are documented in Borgomano et al. (2020).

2.1 Hydrostatic Stress Oscillations

The confining pump, which is connected to the main chamber of the triaxial cell, is able to oscillate around a confining pressure at a frequency of 0.01–1.3 Hz, which is measured using a pressure transducer attached to the main chamber of the triaxial cell using a 1/8″ NPT tube. When a sample is put into the triaxial cell, the hydrostatic pressure

Fig. 1 Top industry triaxial cell: (left) when cell is closed, (right) cell is open, close up on jacketed sample. Modified after Borgomano et al. (2020)

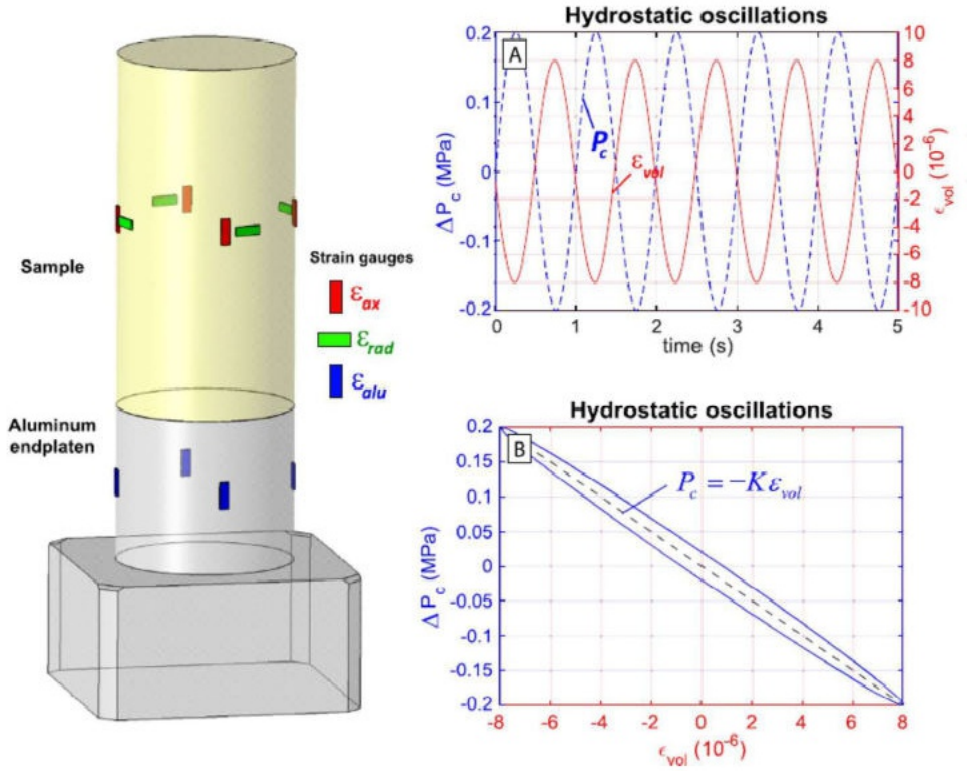

Fig. 2 Strain gauge positions (left) and typical stress–strain recordings of hydrostatic (**a**, **b**) oscillations (around mean values) on a viscoelastic material. The strains (ε_{ax}, ε_{rad}, ε_{alu}) are each averaged from four strain gauges around the circumference of the sample or aluminum end platen at mid-height. Modified after Borgomano et al. (2020)

in the cell is cycled between 5 and 25 MPa three times to ensure all compliant pores are closed. The strain induced by these oscillations are measured using the strain gauges attached to the sample. The magnitude of the confining pressure oscillation is 0.2 MPa to ensure that the strain is within the linear elastic range ($\varepsilon \sim 10^{-6}$) (Winkler and Murphy III 1995). The apparent bulk modulus is calculated as:

$$K = \frac{-\Delta P_c}{\varepsilon_{vol}}, \tag{1}$$

where K is the bulk modulus, ΔP_c is the change in confining pressure and ε_{vol} is the volumetric strain. The volumetric strain is calculated as $2\varepsilon_{rad} + \varepsilon_{axial}$, where ε_{rad} and ε_{axial} are the mean values of all strain gauges glued at mid-height on the sample in the axial and radial directions, respectively (Fig. 2). Using a MATLAB program, fast Fourier transforms (FFTs) are used to determine the stress and strain amplitude for each signal.

2.2 Attenuation (Q^{-1})

In the case of porous rocks, the skeleton of the rock itself is none dispersive. However, the pore fluid diffusion induced by a change in the stress field is time dependent. This can cause dissipation of elastic energy within the sample, similar to that of the rheology of a viscoelastic material (O'Connell and Budiansky 1977). This anelastic behavior is highlighted in Fig. 2B, where the stress–strain curve forms an ellipse, with the area within the ellipse representing the energy lost. This attenuation can be characterized by calculating the phase shift between the stress and the strain, when expressed as a complex stress $\overline{\sigma} = \sigma e^{i(2\pi ft+\phi_\sigma)}$ and complex strain $\overline{\varepsilon} = \varepsilon e^{i(2\pi ft+\phi_\varepsilon)}$ for a dynamic oscillation of frequency f, where ϕ_σ and ϕ_ε are the stress and strain phases.

The stress is related to the strain through its complex modulus $\overline{M}$.

$$\overline{\sigma} = \overline{M}\overline{\varepsilon}. \tag{2}$$

The attenuation factor Q_M^{-1} is then defined as follows (O'Connell and Budiansky 1978):

$$Q_M^{-1} = \frac{\mathrm{Im}\left(\overline{M}\right)}{\mathrm{Re}\left(\overline{M}\right)} = \frac{\mathrm{Im}\left(\overline{\sigma}/\overline{\varepsilon}\right)}{\mathrm{Re}\left(\overline{\sigma}/\overline{\varepsilon}\right)} = \tan\left(\phi_\sigma - \phi_\varepsilon\right). \tag{3}$$

To calculate the Q_M^{-1}, fast Fourier transforms (FFTs) were applied to the stress and strain curves to extract the phases of each, using MATLAB. Using Eqs. (1) and (3) the attenuation of the bulk modulus can be calculated as:

$$Q_{K_{hyd}}^{-1} = \tan\left(\phi_{-\Delta P_c} - \phi_{\varepsilon_{vol}}\right). \tag{4}$$

2.3 Sample Characterization

The sample came from Rustrel in the Urgonian Limestone formation in the SE of France (Borgomano et al. 2019). The Rustrel sample was machined from a core into a cylindrical shape with a diameter of 39 mm and a height of 78 mm (Fig. 3). Using the triple weight method, the porosity, ϕ, of the sample was found to be 16% ± 0.5%. The dry density of the sample is around 2291.5 kg m^{-3}. A thin section was made from a section right above the sample, which was then scanned using a digital microscope (Keyence digital microscope VHX-5000), and a scanning electron microscope (SEM). Figure 3 shows the digital microscope picture (B) which is at a larger scale, with an SEM scan (A) at a smaller scale, as well as pictures of the intact and saw cut samples (C and D). This limestone is made of calcite cement—(b) in Fig. 3A—surrounding micritic peloidal grains—(a) in Fig. 3A—; fragments of rudist shells can also be observed.

The permeability of the intact sample is 3×10^{-17} m^2 at an effective pressure of 7.5 MPa (Table 1). After testing the intact sample, it was then cut down its center, along its length using a diamond saw with a width of 2 mm. The permeability of the saw cut sample was measured at varying confining pressures (2, 6, 10, 14, 18, 22 and 26 MPa) using a constant flow rate at the inlet of 1.5 ml/min and having the outlet pressure at 0 MPa. The effective pressure was then calculated by subtracting half the inlet pressure from the confining pressure.

2.4 Hydraulic Aperture

The hydraulic aperture of the fracture in the saw cut sample is calculated assuming the total flow rate through the sample (Q_w) is equal to the sum of flow rates (i) through the fracture (Q_f) and (ii) through sample matrix (Q_m).

$$Q_w = Q_m + Q_f. \tag{5}$$

Darcy's law states:

$$Q = A\frac{k}{\eta}\frac{\partial P_f}{\partial z}, \tag{6}$$

where k is the permeability (m^2), η is the dynamic viscosity of the pore fluid (Pa s), Q is the flow rate parallel to the fracture (m^3 s^{-1}), A is the area of the sample perpendicular to the flow (m^2) and P_f is the pore fluid pressure (Pa). Equation 6 was used to calculate the permeability.

Equation 6 leads to:

$$k_w A_w = k_m A_m + k_f A_f, \tag{7}$$

where k_w, k_m and k_f are the whole sample, matrix and fracture permeability, respectively, and A_w, A_m and A_f are the whole sample, matrix and fracture areas, respectively.

Apart from the permeability of the fracture, each other term in Eq. 7, is known or is a function of the hydraulic aperture (b) of the fracture. In addition, assuming a parallel

Table 1 Intact Rustrel sample and pore fluid characteristics

Intact parameter	Values
Sample length	L=78 mm
Sample diameter	d=39 mm
Sample's porosity	ϕ=0.16
Sample's permeability	$K=3 \times 10^{-17}$ m^2
Confining oscillation amplitude	P_o=0.2 MPa
Water bulk modulus	K_{wat}=2.2 GPa
Water viscosity	$\eta_{wat}=10^{-3}$ Pa s

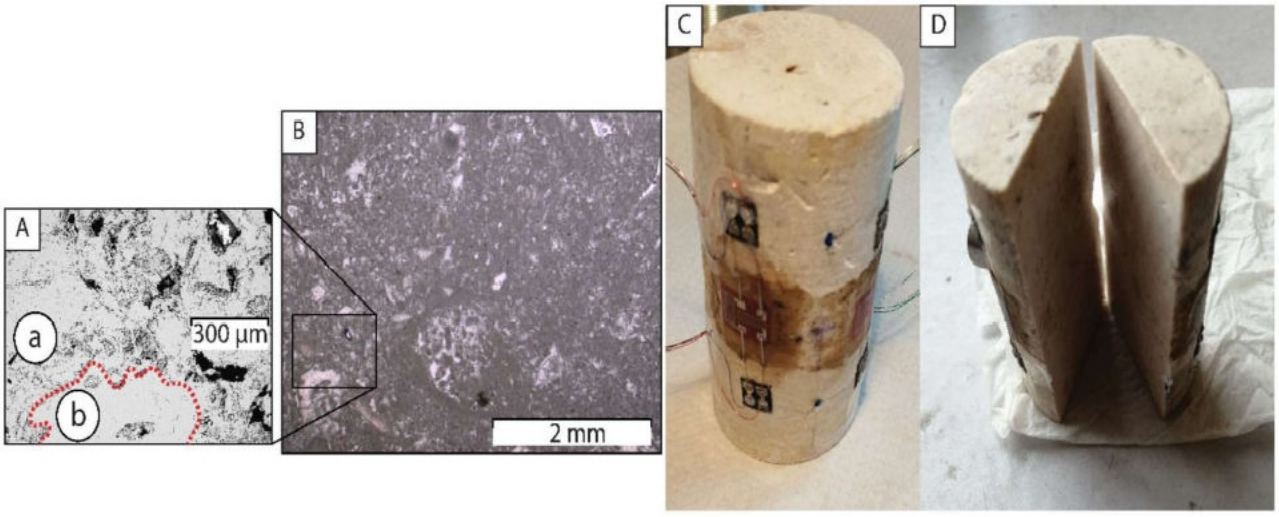

Fig. 3 **A** SEM scan of the thin section; **B** digital microscope picture of the same thin section (using Keyence digital microscope VHX-5000); **C**, **D** intact and saw cut Rustrel samples;

plate model, the permeability of the fracture can also be related to b and:

$$k_f = \frac{b^2}{12}. \tag{8}$$

Using Eqs. 7 and 8, a cubic equation is derived which can be used to infer the hydraulic aperture at varying effective pressures.

2.5 Stiffness of the Fracture

The normal stiffness of a fracture (Z_n) is defined as (Goodman 1976):

$$db = \frac{1}{Z_n}\left(n \cdot d \cdot n + dP_f\right), \tag{9}$$

where n is normal to the fracture and σ the applied stress field. Note that in the case of hydrostatic loading Eq. 9 is simplified as

$$db = -\frac{1}{Z_n}\left(dP_c - dP_f\right) = -\frac{1}{Z_n}dP, \tag{10}$$

where P_c is the confining pressure and P is the effective pressure.

Knowing the hydraulic aperture at several different effective pressures, m, allows approximation of the fracture stiffness at a given effective pressure P_m: the stiffness is calculated between two loading steps P_{m-1} and P_{m+1},

$$Z_n^m = \frac{P_{m+1} - P_{m-1}}{b_{m-1} - b_{m+1}}, \tag{11}$$

where Z_n^m is the stiffness, b_m is the hydraulic aperture measured at the loading step P_m.

Although efforts were made to simplify the geometry of the fracture, it is important to underline that the stiffness is an estimation of the true mechanical aperture as the parallel plate model (Eq. 8) assumes a continuous aperture along the whole fracture, whereas a more realistic geometry would be a fracture with distinct contact areas along the fractures, which is bound to change with increase in effective pressure. Li et al. (2008) showed that as the effective pressure is increased, the difference between mechanical and hydraulic aperture diverge, due to the creation of more complex and tortuous flow paths.

3 Experimental Results

In the first part of this section, the hydraulic aperture, permeability and apparent stiffness of the fracture will be shown. The second part shows the experimental results on the elastic properties of the intact and saw cut samples performed at 5, 10 and 20 MPa of effective pressure saturated with air and water. Figure 4 shows a schematic of the intact and saw cut samples, with the coordinate system used in the next sections.

3.1 Hydraulic Measurements

3.1.1 Saw Cut Fracture Permeability and Hydraulic Aperture

Figure 5 shows, in orange, the permeability of the saw cut sample versus the effective pressure. The figure shows that the permeability decreases as confining pressure is increased, i.e. as the fracture is being closed. The permeability of the sample was measured at seven different effective

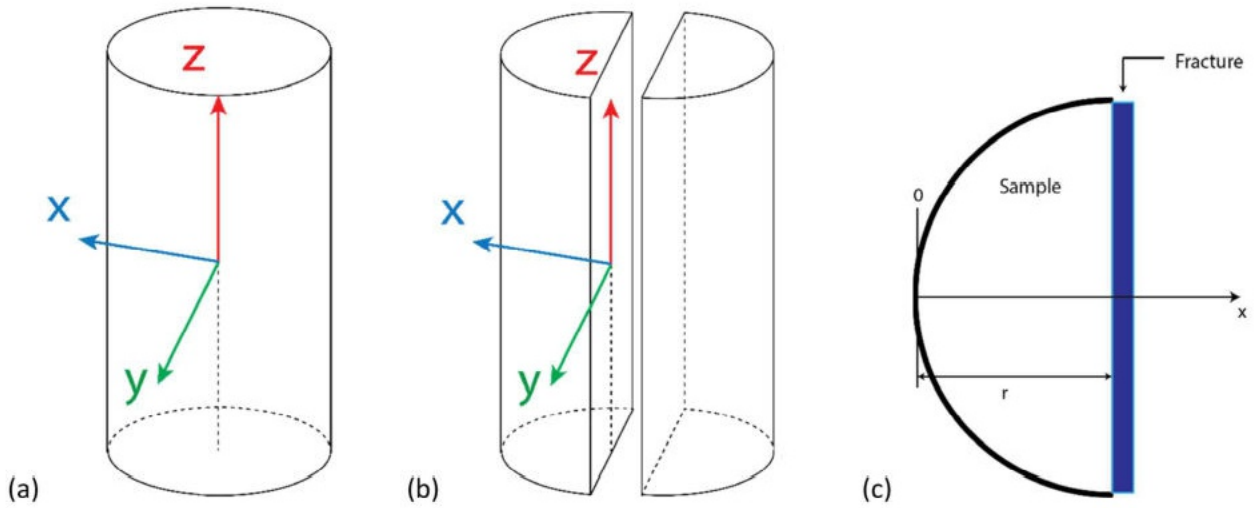

Fig. 4 Intact (**a**) and saw cut (**b**) sample with *xyz* Cartesian coordinate system; (**c**) *xy* representation of saw cut sample

pressures. Within this range, the permeability dropped by 1.4 orders of magnitude as the effective pressure was increased from 1.8 to 22 MPa.

The hydraulic aperture of the fracture was then calculated following the procedure described in Sect. 2.3, within the same effective pressure range and is shown in blue. Within this range, the hydraulic aperture dropped from 14.5 to 5 μm as the effective pressure was increased from 1.8 to 22 MPa. However, the slope of change in hydraulic aperture is much steeper between 1.8 and 11.6 MPa of effective pressure with a drop in hydraulic aperture from 14.5 to 6.0 μm than it is between 11.6 and 22 MPa of effective pressure with a drop in hydraulic aperture from 6.0 to 5.0 μm. This trend shows that the change in permeability and hydraulic aperture due to change of effective pressure mainly occurs for an effective pressure lower than 12 MPa for this specific man-made fracture.

The intact permeability was measured during saturation and was found to be 3×10^{-17} m^2 at an effective pressure of 7 MPa (orange line in Fig. 5). This result is in agreement with the study of Borgomano (2018), who showed that between effective pressures of 2.5 and 20 MPa, the permeability of the Rustrel sample changes slightly from 4×10^{-17} to 2.5×10^{-17} m^2.

3.1.2 Stiffness of the Fracture Versus Effective Pressure

Figure 6 shows, the change in stiffness of the fracture, versus the effective pressure applied to the sample. The stiffness of the fracture was calculated following the procedure described in Sect. 2.4, which also explains the change in number and magnitude of effective pressure points (see Eq. 11). Within this range, the stiffness of the fracture increased from 9.9×10^{11} to 2.0×10^{13} Pa m^{-1} as the effective pressure was increased from 5.3 to 18.4 MPa, which represents an increase of 1.3 orders of magnitude. This figure shows, as expected, that the fracture stiffness is increasing exponentially as the effective pressure is increased. Note that the fracture stiffness is obtained through permeability measurements and under the assumption of a parallel plate model, it is thus a rough estimation of the true fracture stiffness. These results will be compared in the discussion to the fracture stiffness obtained using analytical methods developed further on.

3.2 Hydrostatic Measurements

This sub-section focuses on the results derived from the hydrostatic oscillations, which were performed on the dry and water saturated, intact and saw cut Rustrel sample, at 5, 10 and 20 MPa effective pressures, at a frequency range between 0.04 and 1.1 Hz.

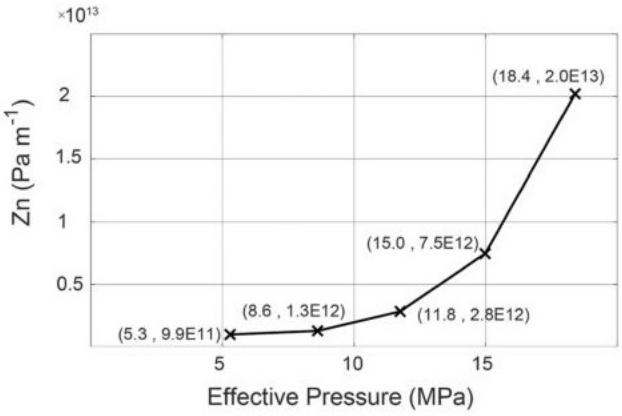

Fig. 6 Normal stiffness of the fracture (Zn) versus effective pressure

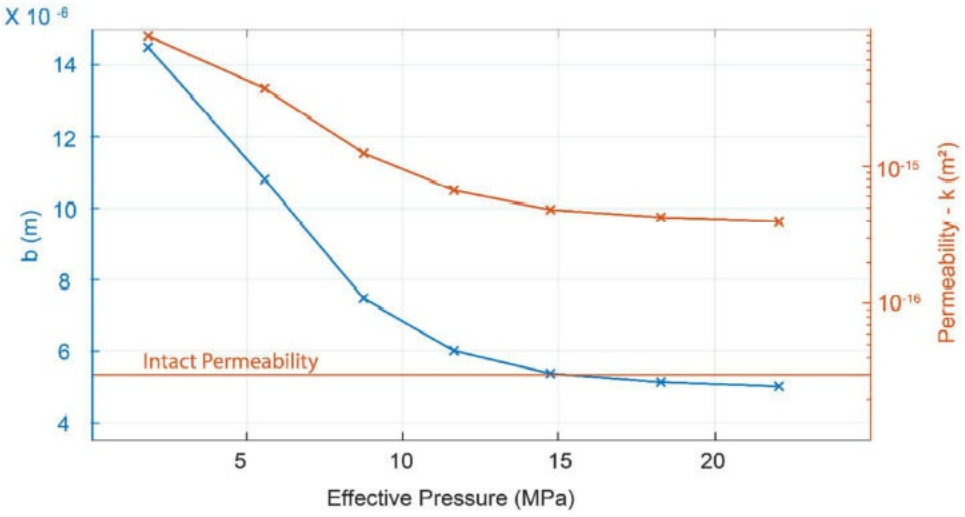

Fig. 5: 1) Left axis: fracture aperture and 2) right axis: permeability log scale versus effective pressure

3.2.1 Hydrostatic Oscillation—Intact Sample

Figure 7 shows the results for the hydrostatic oscillations at 5, 10 and 20 MPa effective pressure, in dry and water saturated undrained conditions, for the intact Rustrel sample. The green and blue crosses represent the dry and water intact data, respectively. The bulk modulus for the dry intact data is constant for all frequencies at 25.3, 25.4 and 26.9 GPa for effective pressures of 5, 10 and 20 MPa, respectively. The attenuation for these are close to 0 and are within the precision of our setup (<0.02). The bulk modulus for the water saturated intact data is constant at all frequencies at around 30.2, 31.1 and 32.6 GPa for effective pressures of 5, 10 and 20 MPa, respectively. The prediction of the water saturated bulk modulus from the dry bulk modulus can be obtained using Gassmann's equation (Gassmann 1951):

$$K_u = K_d + \alpha\left(\frac{\phi}{K_f} + \frac{(-\phi)}{K_s}\right)^{-1}, \tag{12}$$

where K_u and K_d are the undrained and dry moduli, K_f the fluid bulk modulus, K_s the solid mineral bulk modulus, ϕ the porosity and $\alpha = 1 - K_d/K_s$ the Biot coefficient. The predictions of the undrained bulk modulus are given on Fig. 6 (black lines) using a solid mineral bulk modulus of calcite (77 GPa), which is what is observed in the SEM scan, and are in good agreement with the measured undrained bulk modulus.

3.2.2 Hydrostatic Oscillation—Saw Cut Sample

Figure 8 shows the results for the hydrostatic oscillations at 5, 10 and 20 MPa effective pressure, in dry and water saturated conditions, for the saw cut Rustrel sample. The green and blue Xs represent the dry and water saw cut data, respectively. The apparent bulk modulus is shown in the top half and the phase shift is shown in the bottom half. The apparent bulk modulus is calculated in the same way as the bulk modulus for the intact sample. This bulk modulus is not the bulk modulus of the fractured sample, as strains are measured locally by strain gauges glued on the matrix. This apparent bulk modulus is the bulk modulus of the matrix (or background) affected by pore pressure changes induced by the fracture. The phase shift is calculated in the exact same way as for the bulk attenuation for the intact sample, however, since the strain measurements are local, it is not the attenuation of the fractured sample, but a phase shift between strain and stress due to the time delay for pore fluid to flow from the fracture to the matrix.

The apparent bulk modulus for the dry saw cut data is constant for all frequencies at 26.7, 28 and 28 GPa for effective pressures of 5, 10 and 20 MPa, respectively. The error band shown in Fig. 8 is defined using the mean and standard deviation of the dry saw cut phase shift data and is within the typical precision (<0.02) found for dry samples in this setup. This is used to compare to the water saturated data. The bulk moduli for the dry saw cut sample are very close to those obtained in the intact sample; indeed, the bulk modulus is

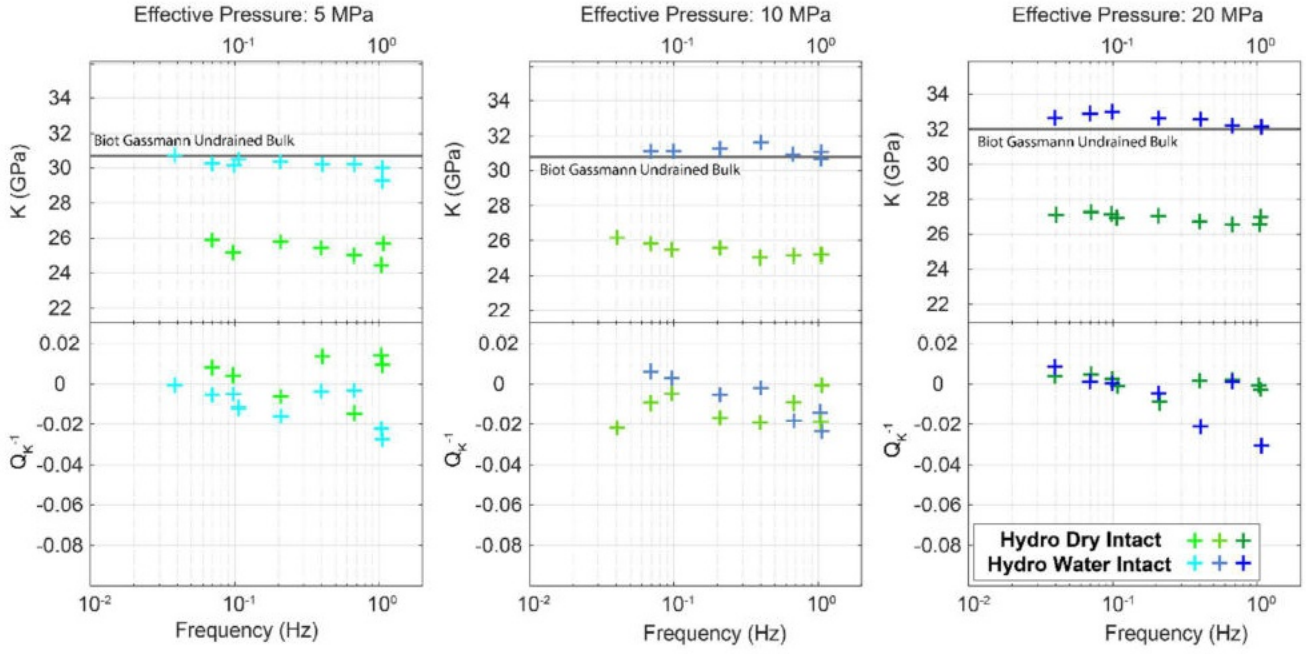

Fig. 7 Intact Rustrel's dry and water bulk moduli and attenuation at 5, 10 and 20 MPa P_{eff} for axial oscillations. In addition, the prediction of the undrained bulk modulus from Gassmann's equation is plotted. A good match is found between the prediction of Gassmann's equation and the measured undrained bulk moduli

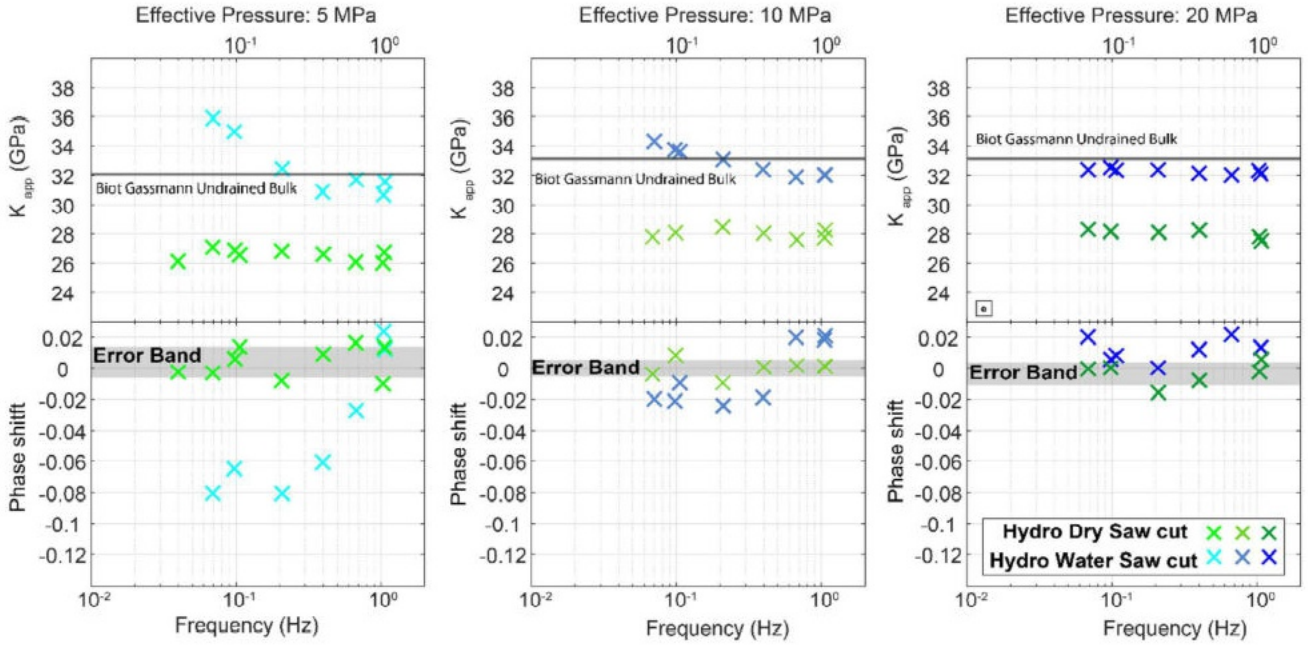

Fig. 8 Saw cut Rustrel's dry and water saturated bulk modulus and phase shift between stress and stain at 5, 10 and 20 MPa P_{eff} for hydrostatic oscillations;

obtained from strain gauges glued on the rock: it is a local measurement.

Under water saturation and for 5 MPa effective pressure, the apparent bulk modulus reaches a peak at the lowest frequency of 0.07 Hz with a value of 36 GPa. The value for the apparent bulk modulus decreases with increasing frequency until 0.4 Hz, at which point it stabilizes around 31 GPa. The phase shift between the stress and strain is negative at low frequencies, with values around − 0.08, and increases to 0 at 1 Hz. For 10 MPa effective pressure, again the apparent bulk modulus is at its peak at the lowest frequency of 0.07 Hz with a value of 34.3 GPa. This value decreases with increasing frequency until 0.4 Hz at which point it stabilizes around 32 GPa. The phase shift between stress and strain is negative at low frequencies, with values around − 0.02 and increases to 0 at 1 Hz. For 20 MPa effective pressure, the apparent bulk modulus is constant for the full frequency range and there is no attenuation. The dry bulk modulus of the matrix in the saw cut sample is slightly larger by ~ 1 GPa, than the one measured in the intact sample. This might be due to the extra hydrostatic cycling that the saw cut sample was imposed at the start of every triaxial test, which is common practice to close microcracks; but note that it is also in the error bar of the bulk modulus (~ 1 GPa).

4 Modeling for the Saw Cut Samples

Theoretical models of dispersion due to wave-induced fluid flow between pores and fractures have been developed based on poroelasticity theory (Chapman 2003; Brajanovski et al. 2005; Gurevich et al. 2009). These models show that the characteristic frequency of dispersion depends on the matrix permeability, fluid viscosity, as well as the fracture geometry and properties. The aim, here, is to model the experiment, and in particular the fact that measurements are local measurements obtained by strain gauges, which has not been developed analytically to the authors' knowledge. The present approach is consistent with the theory of poroelasticity and, as in the work of Brajanovski et al. (2005), the mechanism behind the dispersion is fluid flow induced between the matrix and the fracture.

4.1 Pore Pressure

Here, we develop a 1D analytic solution along x within the frequency domain (Fig. 4c). A mass balance and mechanical equilibrium equation for a linear isotropic poroelastic homogeneous medium, leads to a partial differential equation which involves the pore fluid pressure (e.g. Rice and Cleary 1976; Zimmerman 2000; Guéguen and Boutéca 2004):

$$\frac{\partial p_f}{\partial t} - \frac{kBK_d}{\eta\alpha(1-\alpha B)}\nabla^2 p_f + \frac{BK_d}{1-\alpha B}\frac{\partial \varepsilon_v}{\partial t} = 0, \tag{13}$$

where k, K_d, B, p_f, α and ε_v are the rock's permeability, drained bulk modulus, Skempton's coefficient, pore fluid pressure, Biot's coefficient and the volumetric strain, respectively.

The oscillating hydrostatic pressure is applied so that $P_c(t)$ is sinusoidal and time dependent ($P_c(t) = P_o e^{i\omega t}$). Again, the pore fluid pressure is dependent on the location x (1D model), as well as being time dependent, $p_f(x,t) = f(x)e^{i\omega t}$. Substituting the oscillating hydrostatic pressure and pore fluid pressure equations into Eq. 13 leads to:

$$f''(x)\frac{ik}{\eta S\omega} + f(x) = BP_o, \tag{14}$$

where S is the rock's storage coefficient ($S = \alpha/(BK_d)$). Using the fluid hydraulic diffusivity ($D = k/(S\eta)$), the previous equation can be rewritten as:

$$f''(x)\frac{iD}{\omega} + f(x) = BP_o. \tag{15}$$

The boundary conditions, at $x=0$ (at the jacket) and $x=r$ (at the fracture), are used to solve this problem. At $x=0$, fluid is not allowed to flow out of the sample, which leads to:

$$\left.\frac{\partial P_f}{\partial x}\right|_{x=0} = 0. \tag{16}$$

The second boundary condition states that there is a mass balance between the pore fluid leaving the pore space in the sample and the pore fluid entering the fracture which happens at $x=r$. The mass of pore fluid, m, flowing from the sample to the fracture is given by Darcy's law:

$$\left.\frac{\partial m}{\partial t}\right|_{x=r} = -\rho\frac{kA}{\eta}\left.\frac{\partial P_f}{\partial x}\right|_{x=r}, \tag{17}$$

where ρ is the fluid density and A is the surface area of the fracture in the y–z plane. The change of pore fluid mass in the fracture is related to the pore fluid pressure, and the volume change of the fracture:

$$\frac{\partial \rho V}{\partial t} = \rho\frac{V}{K_f}\frac{\partial P_f}{\partial t} + \rho\frac{\partial V}{\partial t}, \tag{18}$$

where V is half of the fracture volume and K_f the fluid bulk modulus. The volume change of the fracture is related to the change in its aperture, b, and can be expressed as $dV = Adb/2$. In addition db is related to the fracture's normal stiffness, Z_n (Eq. 10).

Thus combining 17, 18 and 10, leads to the boundary condition at $x=r$:

$$S_1\left.\frac{\partial P_f}{\partial t}\right|_{x=r} - \frac{A}{2Z_n}\left.\frac{\partial P_c}{\partial t}\right|_{x=r} + \frac{kA}{\eta}\left.\frac{\partial P_f}{\partial x}\right|_{x=r} = 0, \text{ with } S_1 = \frac{V}{K_f} + \frac{A}{2Z_n}\frac{A}{2Z_n}. \tag{19}$$

In the estimation of S_1, the compressibility of the fluid can be neglected in comparison to the fracture stiffness. Using both boundary conditions, the pore fluid pressure $p_f(x,t)$ can be solved:

$$P_f(x,t) = P_o e^{i\omega t}\left(B + \cosh\sqrt{\frac{i\omega}{D}}x\left[\frac{1-B}{2Z_n S\sqrt{\frac{D}{i\omega}}\sinh\sqrt{\frac{i\omega}{D}}r + \cosh\sqrt{\frac{i\omega}{D}}r}\right]\right). \tag{20}$$

Equation 20 highlights the characteristic frequency $f_f \propto \frac{D}{r^2}$, which is the time needed for the pore pressure to equilibrate between the fracture and pores (Brajanovski et al. 2005).

In the limit case of low frequency $w \to 0$, Eq. 20 reduces to:

$$P_f(x,t) = P_o\left(B + \frac{1-B}{1+2SZ_n r}\right). \tag{21}$$

In this case, frequencies are low enough to allow equilibration of the fluid pressure between fracture and pores.

In the limit case of high frequency $\omega \to \infty$, Eq. 20 reduces to:

$$P_f(x<r,t) = BP_o e^{i\omega t} \text{ and } P_f(r,t) = P_o e^{i\omega t}. \tag{22}$$

At high frequencies, the fluid has no time to move from pores in the matrix into the fractures, or vice versa. In this case the pore pressure in the matrix (related to the Skempton coefficient) is lower than the pore pressure in the fracture.

Figure 9a shows the evolution of the pore pressure in the sample during hydrostatic oscillations, using Eq. 20, from $x=0$ to r, at frequencies of 10^{-4}, 10^{-1}, 10^{0}, 10^{1} and 10^{4} Hz. The sample characteristics used for this model are given in Table 2. At a frequency of 10^4 Hz, the pore pressure in the sample is constant at $p_f = B\Delta P_c = 53$ kPa and the pore pressure in the fracture reaches $\Delta P_c = 0.2$ MPa. As the frequency of the applied stress oscillations is reduced, the pore pressure in the fracture decreases, indeed the pressure has time to percolate through the sample, causing a higher

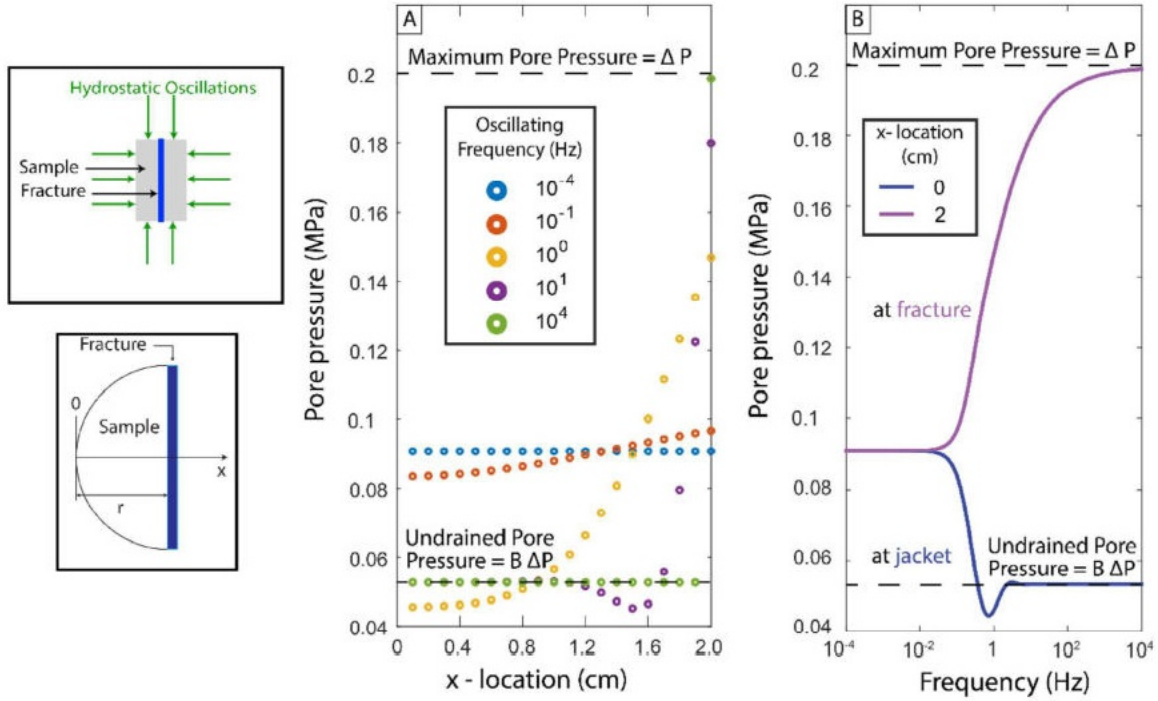

Fig. 9 Pore pressure versus x-location and pore pressure versus frequency (at $x=0$ and 2 cm)

Table 2 1D model sample characteristics

Sample characteristics for 1D model	Values
Stiffness of fracture—Z_n (m Pa^{-1})	0.75×10^{12}
Dry bulk modulus—K_d (GPa)	26
Matrix permeability—k (m^2)	10^{-17}
Porosity—ϕ	0.16
Skempton's coefficient—B	0.2407

pore pressure throughout the sample matrix. The pore pressure found near the jacket (at $x=0$) is found to be 53 kPa, when the applied frequency is 10^4 Hz. As the frequency is reduced to quasi static conditions, the pore pressure found near the jacket increases to its highest value of 90.7 kPa (using Eq. 22). Figure 9B shows the pore pressure evolution versus frequency at $r=0$ (where strain gauges are glued) and 2 cm (inside the fracture). At low frequencies, the pore pressure in the whole sample is equilibrated and equal to 90.7 kPa, then as the frequency is increased, the pore pressure decreases at the strain gauge location and increases in the fracture.

4.2 Apparent Bulk Modulus

Recalling that the volumetric strain is given by:

$$\varepsilon_v(x,t) = -\frac{1}{K_d}\left[P_c(t) - \alpha p_f(x,t)\right]. \tag{23}$$

The local apparent bulk modulus measured by the strain gauge at $x=0$ is calculated using Eq. 20:

$$K_{matrix} = -\frac{P_o e^{i\omega t}}{\varepsilon_v(0,t)} = \frac{K_d}{\left\{1-\alpha\left(B+\left[\frac{1-B}{2Z_n S\sqrt{\frac{D}{i\omega}}\sinh\sqrt{\frac{i\omega}{D}}r+\cosh\sqrt{\frac{i\omega}{D}}r}\right]\right)\right\}}. \tag{24}$$

In the limit case of high frequency ($\omega \to \infty$),

$$K_{matrix} = \left[\frac{K_d}{1-B\alpha}\right] = K_u, \tag{25}$$

which is simply the undrained bulk modulus. In this limit case, the bulk modulus measured by the strain gauge is not affected by the fracture.

In the limit case ($\omega \to 0$), the local apparent bulk modulus is:

$$\frac{1}{K_{\text{matrix}}} = \frac{1}{K_{\text{u}}} - \frac{\alpha(1-B)}{K_{\text{d}}\left(1+2SZ_{\text{n}}r\right)}. \tag{26}$$

In this case, the bulk modulus measured by the strain gauge is larger than the undrained bulk modulus, as the pore pressure in the matrix is higher.

4.3 Bulk Modulus of the Fractured Sample

The overall goal here is not to develop a complete model for P-wave dispersion of a porous rock containing a fracture. Such analytical models can be found in Chapman (2003) or Brajanovski et al. (2005). Here, the aim is to show that a negative phase shift for the apparent bulk modulus predicted in Sect. 4.2 is in agreement with a positive bulk attenuation of the fracture sample. First of all, as the matrix is an isotropic elastic solid, the fractured sample is a transversely isotropic elastic solid. However, it is still possible to define a bulk modulus of the fracture sample, K_{fr}, defined as:

$$P - P_{\text{f}} = -K_{\text{fr}}\frac{\Delta V}{V}, \tag{27}$$

where V is the volume of the fractured sample.

Let us consider the bulk modulus, K_{fr}, of the fractured sample in the fluid-saturated case, in the limit case of high frequency $w \to \infty$ Eqs. 10, 25 and 27 leads to

$$K_{\text{fr}} = K_{\text{u}}, \tag{28}$$

which is the same as if there was no fracture; in agreement with previous results (Brajanovski et al. 2005).

Let us consider the bulk modulus, K_{fr}, of the fractured sample in the fluid-saturated case, in the limit case of low frequency $w \to 0$ Eqs. 10, 26 and 27 leads to

$$\frac{1}{K_{\text{fr}}} = \frac{1}{K_{\text{u}}} - \frac{\alpha(1-B)^2}{K_{\text{d}}B\left(1+2SZ_{\text{n}}r\right)} = \frac{1}{K_{\text{u}}} - \frac{\alpha(1-B)^2}{K_{\text{d}}B+\alpha 2Z_{\text{n}}r}. \tag{29}$$

Figure 10 shows in solid and dashed lines the theoretical predictions of the apparent matrix bulk modulus (at $x=0$) and the bulk modulus of the fractured sample for different

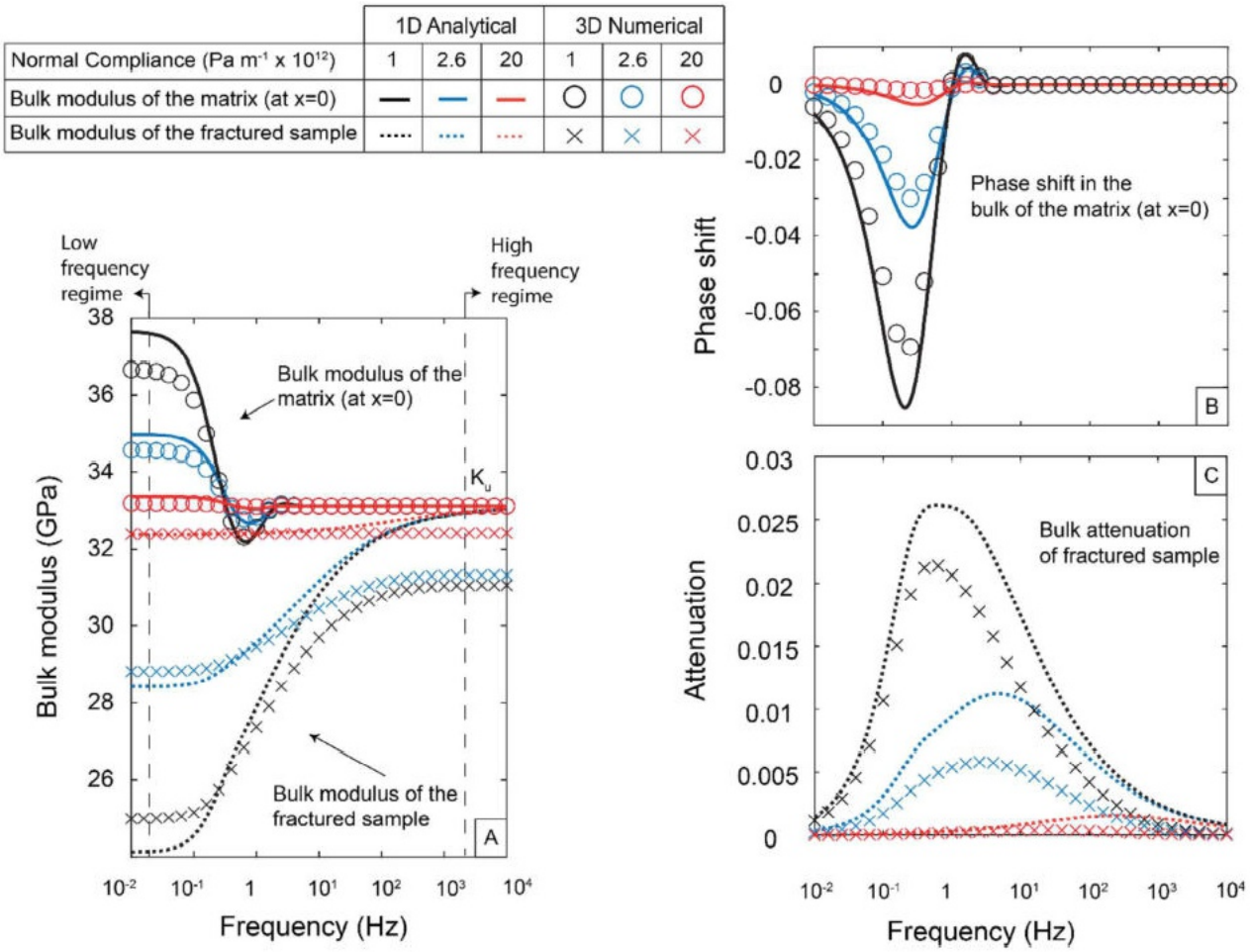

Fig. 10 Bulk Modulus of local measurement ($x=0$) and of whole fractured sample versus frequency, with associated phase shift and attenuation versus frequency

Table 3 Material properties for the poroelastic equations used in COMSOL multiphysics, with bulk and shear modulus shown for 3 different scenarios similar to effective pressures of 5, 10 and 20 MPa, respectively

	Intact	Fracture
Grain bulk modulus (GPa)	$K_s = 77$	$K_s = 77$
Grain density (kg/m^3)	$\rho_s = 2710$	$\rho_s = 2710$
Porosity	$\phi = 0.16$	$\phi = 0.9$
Permeability (m^2)	$k = 10^{-17}$	$k = 10^{-12}$
Drained bulk modulus (GPa)	$K_d = 28$	$K_d = 0.2, 0.52, 4$
Drained shear modulus (GPa)	$\mu_d = 14$	$\mu_d = 0.1, 0.26, 2$
Fluid bulk modulus (GPa)	$K_f = 2.2$	$K_f = 2.2$
Fluid density (kg/m^3)	$\rho_f = 1000$	$\rho_f = 1000$
Fluid viscosity (Pa s)	$\eta_{wat} = 10^{-3}$	$\eta_{wat} = 10^{-3}$

value of the normal fracture compliance and using the poroelastic constants given in Table 3. At high frequency, the moduli are not affected by the fracture and converge to the undrained bulk modulus. As the frequency increases the bulk modulus of the fracture sample increases, in agreement with Brajanovski et al. (2005). The trend of the apparent bulk modulus of the matrix shows an opposite trend which decreases as the frequency increases. Note that using the low-frequency bulk modulus value, and Eqs. 26 or 29 it is possible to directly infer the fracture compliance, knowing the poroelastic properties of the rock.

One needs to remember that the evolution of the apparent matrix bulk modulus is related to the pore fluid migrating from the fracture to the pore volume. This creates theoretically an unusual negative phase shift between stress and strain (Fig. 10b), which is not seen when looking at the attenuation of the bulk modulus of the fractured sample (Fig. 10c).

4.4 1D Analytical Versus 3D Computational

The 1D analytical model allows to understand the mechanisms behind the dispersion and attenuation of the apparent matrix bulk modulus. However, the 1D model is a geometrically simplified version of the fractured cylindrical sample. To take into account the 3D geometry of the experiment, the dispersion and attenuation caused by the fluid pressure diffusion is modelled numerically in COMSOL by solving Biot's (1941) poroelastic quasistatic equations in the frequency domain, using the displacement–pressure formulation (Quintal et al. 2011). These equations are:

$$\nabla \cdot \sigma = 0, \tag{30}$$

$$\nabla \cdot \left(-\frac{k}{\eta} \nabla p_f \right) + \alpha \nabla \cdot (i\omega u) + \frac{I\omega p}{M} = 0, \tag{31}$$

where u is the vector of solid displacement, with components in the x, y and z directions, and σ is the stress tensor,

$$\sigma_{ij} = 2\mu\varepsilon_{ij} + \lambda e\delta_{ij} - \alpha p\delta_{ij}, \tag{32}$$

where δ_{ij}, ε_{ij} and e are the Kronecker delta, components of the strain tensor and cubical dilation given by the strain tensor, respectively. The μ and λ are the shear modulus for the dry frame and Lamé's parameter $\lambda = K_d - 2\mu/3$. The coefficient M is (Biot and Willis 1957)

$$M = \left(\frac{\phi}{K_f} + \frac{\alpha - \phi}{K_s} \right)^{-1}. \tag{33}$$

The fractured sample is modeled with an intact matrix and a fracture having a higher permeability, porosity and compliance. The drained bulk modulus for the fracture was calculated using the normal stiffness of the fracture multiplied by the aperture. We also take into account a fracture shear modulus, estimated and taken as half the value of the drained bulk modulus, according to the study of Lubbe et al. (2008) on a carbonate limestone. The geometry is made of two half cylinders (matrix), with a rectangular cuboid in between both halves (fracture). The width of the rectangular cuboid is equal to the diameter of the cylinder at 40 mm. The height of the fracture is equal to the height of the cylinder and was taken as 80 mm. The fracture aperture has little effect in the analytical model or numerical model as long as the aperture is smaller than 1.1×10^{-3} m (Eq. 29) and sensitivity tests were done on the effect of aperture. The model was run at an aperture of 2×10^{-4} m with sensitivity tests run at 10^{-6} m. The parameters used for the intact and fracture volumes are summarized in Table 3.

COMSOL multiphysics is used to create a volumetric mesh with tetrahedral elements and the weak form of Eqs. 31 and 32 are solved, using a finite element method. The gradient of fluid pressure is set to 0 along the outside boundary, creating undrained boundary conditions. To induce the hydrostatic pressure, an oscillatory radial stress amplitude of 2×10^5 Pa is applied along the curved surface of the cylinder and fracture. An oscillatory stress amplitude of 2×10^5 Pa is applied to the top of the cylinder in the negative z direction and to the bottom of the cylinder in the positive z direction.

Figure 10 shows the 1D analytical solution and 3D COMSOL multiphysics results of the apparent matrix bulk modulus (at location $x = 0$) and the bulk modulus of the fracture sample versus frequency, for 3 fracture stiffness's: 1×10^{12}, 2.6×10^{12} and 2×10^{13} Pa m^{-1}. The solid and dashed lines show the 1D analytical model results. The Os and Xs are for the 3D numerical model completed in COMSOL multiphysics. The solid line and Os are for local measurements at the "strain gauge" location. The dashed line and Xs are for global measurements, i.e. matrix and fracture. The black,

blue and red colors represent the solution at a normal compliance of 1, 2.6 and 20 × 10^{12} Pa m^{-1}, respectively.

In the low-frequency regime, below 10^{-2} Hz, the bulk modulus of the fractured sample is smaller than the apparent matrix bulk modulus. In the high-frequency regime above 10^{3} Hz, the apparent matrix bulk modulus are equal and constant at K_u (Eq. 25). Overall, there is a good consistency between the 1D model and the 3D numerical model: for the apparent matrix modulus, the low-frequency moduli for the 1D analytical model are 37.6, 35 and 33.2 GPa for a fracture stiffness of 1 × 10^{12}, 2.6 × 10^{12} and 2 × 10^{13} Pa m^{-1}, respectively, whereas for the 3D numerical model these values are 36.7, 34.6 and 33.2 GPa. For the bulk modulus of the fractured sample, the low-frequency moduli for the 1D analytical model are 24.1, 28.4 and 32.8 GPa for a fracture stiffness of 1 × 10^{12}, 2.6 × 10^{12} and 2 × 10^{13} Pa m^{-1}, respectively, whereas for the 3D numerical model, these values are 25, 28.8 and 32.4 GPa.

The critical frequency for the attenuation for the 1D analytical model and 3D analytical model also match well. The amplitude of the attenuation (fractured sample) for the 1D analytical model are 0.026, 0.011 and 0.001 for fracture stiffness of 1 × 10^{12}, 2.6 × 10^{12} and 2 × 10^{13} Pa m^{-1}, respectively, whereas for the 3D numerical model, these values are 0.021, 0.006 and 0.000. The amplitude of the phase shift (apparent matrix modulus) for the 1D analytical model is − 0.085, − 0.038 and − 0.005 for a fracture stiffness of 1 × 10^{12}, 2.6 × 10^{12} and 2 × 10^{13} Pa m^{-1}, respectively, whereas for the 3D numerical model, these values are − 0.069, − 0.0307 and − 0.001.

Small differences between the 1D and 3D models are expected as the solution for pore pressure propagation in the 3D numerical model is more intricate, taking into account the complex geometry of the sample, whereas the 1D analytical model is simplistic. That being underlined, the critical frequency is the same for both the 1D and 3D models, both models predict almost the same negative phase shift for the apparent matrix bulk modulus, and both models show an apparent matrix bulk modulus that converges at K_u in the high-frequency regime.

In the high frequency, and for the fractured sample, the modulus converges to a value smaller than K_u for the 3D simulation. This is due to the aperture not being small enough: when modelling with a smaller aperture (10^{-6} m), the 3D numerical model converges to K_u, which is not shown, since the length of the sample has to be greatly reduced to create a model that could be run on the servers without crashing the system. This is further highlighted by the increase in high-frequency apparent matrix bulk modulus, with an increase in fracture stiffness, as the fracture stiffness comes closer to the matrix stiffness.

4.5 Comparing Experimental Results with the 1D Analytical Model

Figure 11 shows the results presented in Fig. 7, with the solution to the 1D analytical model, as well as the solution for the 3D numerical model. The sample properties for the 1D and 3D models can be seen in Table 4. The drained bulk modulus is taken from Fig. 7. The fracture stiffness was calculated using the low-frequency regime (Eq. 26) for the 1D

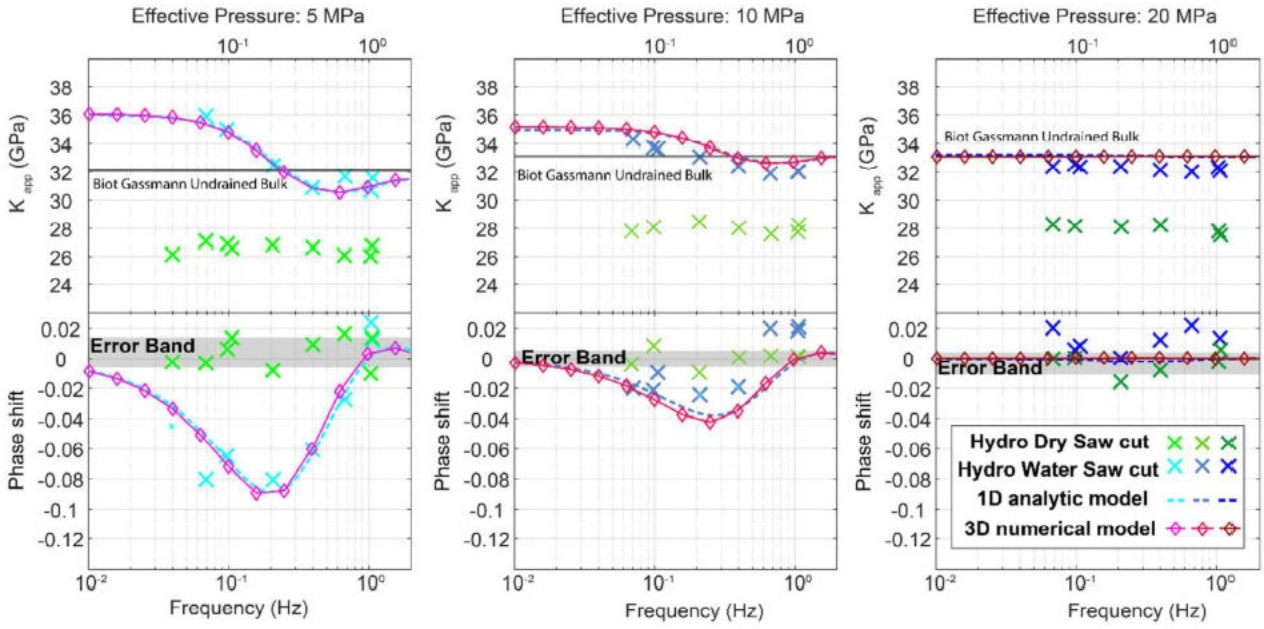

Fig. 11 Experimental results for hydrostatic oscillations with the predictions of the 1D model superimposed;

Table 4 1D and 3D model sample characteristics

Sample characteristics	Sample effective pressure (MPa)					
	1D analytical			3D computational		
	5	10	20	5	10	20
Stiffness of fracture—Z_n(Pa m^{-1})	1×10^{12}	2.6×10^{12}	5×10^{13}	0.7×10^{12}	1.8×10^{12}	3.5×10^{13}
Drained bulk modulus—K_d (GPa)	26	28	28	26	28	28
Matrix permeability—k (m^2)	10^{-17}					
Porosity—ϕ	0.16					

analytical model, and was adjusted, in the 3D model, to fit the experimental data (it is the only unknown parameter).

Figure 11 shows that the experimental data are in good agreement with the 1D analytical and 3D numerical models. The inferred value for the fracture stiffness are given in Table 4. The fracture stiffness increases as effective pressure increases. The 1D and 3D models predict the same order of magnitude for the fracture stiffness, however, the 1D model slightly overestimates the fracture stiffness, and for the three effective pressures a ratio of ~ 0.7 is found between the fracture stiffness used from the 3D model to the one deduced from the 1D model. As the 3D model takes into account the geometry of the problem, it is probably a better approximation of the stiffness of the fracture. The 1D model is analytical, catches the mechanisms behind dispersion and attenuation, and is easy to use to interpret the experimental data.

5 Discussion

In this paper, the permeability of the sample was used to calculate the hydraulic aperture of the fracture. For a saw cut sample with the fracture running parallel to the flow path, there is an expected decrease in permeability when the effective pressure is increased, which has been shown experimentally by others (Kluge et al. 2017; Blöcher et al. 2019) and is consistent in this work. The flow rates used for the hydraulic aperture never exceeded 2.5×10^{-8} m^3/s, which is well below the Reynolds number threshold for laminar flow and the fracture is relatively flat and parallel as it was cut using a diamond saw, however, there is certainly partial contact between both halves of the sample, meaning the parallel plate model is not completely met. The stiffness of the fracture calculated using this method has an error of 1, 33 and 92%, at effective pressures of 5, 10 and 20 MPa, when compared to the stiffness calculated from the 1D analytical model, and 41, 4 and 26% when compared to the fracture stiffness from the 3D numerical model. The 3D numerical model is in better agreement with the hydraulic measurements of fracture stiffness, than the 1D analytical model. Li et al. (2008) showed that the error between hydraulic aperture and real aperture are on an order of 2.

The pore pressure model presented in Sect. 4.2, shows the trend of pore pressure along the x axis depending on the applied hydrostatic frequency. The pore pressure in the pore matrix is highest at low frequencies and lowest at high frequencies, the opposite is true for the fluid pressure in the fracture. At high frequencies (10^3 Hz and above), the pore pressure in the fracture does not have time to dissipate into the matrix. This is analogous to squirt-flow attenuation mechanisms, for which fluid does not have the time to equilibrate between pores and cracks. Note, however, that in the case of a fracture medium, poroelasticity can be applied as the pore pressure is equilibrated at a REV scale, which is not the case for squirt flow. In addition, the cut-off frequency related to squirt flow is typically at a much higher frequency range (> 10 kHz), whereas in this case, the frequency cut-off is:

$$f \approx \frac{4D}{L^2}, \tag{34}$$

where L is the distance between two fractures (or two times the distance r in our experiments), and thus typically occurs at low frequency. The distance between the fractures (and thus the fracture density) is a key parameter to estimate the frequency cut-off. This can be shown by using the 1D analytical model developed and changing the value of r. When changing r from 2 to 4 to 8 cm, the cut-off frequency goes from 0.85 to 0.32 to 0.12 Hz with the attenuation magnitude going from 0.076 to 0.048 to 0.025, respectively. This is consistent with the numerical models developed by Hunziker et al. (2018) which has shown that an increase in fracture density does increase the magnitude and cut-off frequency of the attenuation caused by FPD from the fracture to the pore space.

Figures 10 and 11 show that the critical frequency for the FPD from the fracture to the matrix changes depending on the fracture stiffness, with an increase in critical frequency as the fracture stiffness increases. The importance of the location of the strain measurement is highlighted in Fig. 10, the local strain measurement shows a critical frequency which is smaller than that of the critical frequency for the whole sample. The importance of the location of strain measurement has been shown numerically before by

Chapman and Quintal (2018), with a change in the cut-off frequency depending on the location of where the strain measurement was taken. A negative phase shift was also shown in their work, when the attenuation was measured locally at a set distance from a fracture. This negative phase shift is shown experimentally in Fig. 11, at lower effective pressures, as the strain gauges used here are local measurements, which shows the effect the fracture has on the local strain measurements. The 'global' bulk strain measurements would be needed, to calculate directly the bulk dispersion and attenuation of the fractured sample. The 1D model in this paper (Fig. 11), as well as the numerical model in Chapman and Quintal (2018), show that although some local measurements can create a negative phase shift between the stress and strain, the 'global' bulk attenuation is still positive. However, this work shows that it is possible to calculate the fracture stiffness by inversion through the apparent matrix bulk modulus, and then predict the bulk modulus and attenuation of the fractured sample.

The dispersion caused by the fracture decreases in magnitude with an increase in effective pressure. This is expected as the fracture closes when there is an increase in effective pressure. When using the 1D model, the amplitude of the attenuation is sensitive to the stiffness of the fracture, which decreases with an increase of effective pressure. This implies that dispersion and attenuation related to fractures mainly occurs in shallow reservoirs, or during fluid injection as the effective pressure is increased leading to opening of pre-existing fractures.

6 Conclusion

With the addition of innovative microvalves, a set of hydrostatic oscillation tests was performed on an intact and saw cut cylindrical sample at frequencies between 0.07 and 1 Hz in purely undrained conditions. As expected, the intact sample showed no dispersion for dry or water saturated conditions. Permeability tests were performed at a large range of effective pressures to measure hydraulic aperture and stiffness of the man-made fracture. Using the local strain measurements during the hydrostatic oscillations, the apparent matrix bulk modulus and phase shift were measured. At an effective pressure of 5 MPa, the apparent matrix bulk modulus decreased from 36 at low frequency to stabilize at 31 GPa at higher frequencies and a maximum local negative phase shift of − 0.08 was recorded, with the cut-off frequency at ~ 0.2 Hz. At an effective pressure of 15 MPa, the local bulk modulus again decreased with increase in frequency, however only by 2.6 GPa from 34.6 to 32 GPa and a maximum local negative phase shift of − 0.02 was recorded, with a cut-off frequency at ~ 0.35 Hz. At an effective pressure of 20 MPa, there was no change in local bulk modulus and no phase shift.

A 1D analytical model and 3D numerical model, for hydrostatic oscillations on a fractured sample, were developed and fit well the experimental data, which implies a fracture to matrix leak-off. The models give insight on how a negative phase shift can be observed locally, and how the fracture stiffness can be measured. It underlines also the importance of fracture stiffness and the location of the strain measurements on the cut-off frequency and the magnitude of the phase shift.

Acknowledgements This work has been supported by TOTAL, under the project FR00009778. The authors would like to thank TOTAL for allowing publication of these results. We would also like to thank D. Deldicque for his expertise on the SEM photomicrographs.

Author Contributions Conceptualization: AG, JF and JB; methodology: AG and JF; formal analysis and investigation: AG and JF; writing—original draft preparation: AG; writing—review and editing: AG and JF; funding acquisition: JF; resources: JF; supervision: JF and JB; development of analytical model: JF and AG; development of numerical model: AG.

Funding This work has been supported by TOTAL, under the project FR00009778. We would like to thank TOTAL for allowing publication of these results.

References

Adelinet M, Fortin J, Guéguen Y (2011) Dispersion of elastic moduli in a porous-cracked rock: Theoretical predictions for squirt-flow. Tectonophysics 503(1–2):173–181. https://doi.org/10.1016/j.tecto.2010.10.012

Amalokwu K, Best AI, Sothcott J, Chapman M, Minshull T, Li XY (2014) Water saturation effects on elastic wave attenuation in porous rocks with aligned fractures. Geophys J Int 197(2):943–947. https://doi.org/10.1093/gji/ggu076

Bailly C, Fortin J, Adelinet M, Hamon Y (2019) Upscaling of elastic properties in carbonates: a modeling approach based on a

multiscale geophysical data set. J Geophys Res Solid Earth 124(12):13021–13038. https://doi.org/10.1029/2019JB018391

Barbosa ND, Caspari E, Rubino JG, Greenwood A, Baron L, Holliger K (2019) Estimation of fracture compliance from attenuation and velocity analysis of full-waveform sonic log data. J Geophys Res Solid Earth 124(3):2738–2761. https://doi.org/10.1029/2018JB016507

Batzle ML, Han DH, Hofmann R (2006) Fluid mobility and frequency-dependent seismic velocity—direct measurements. Geophysics 71(1):N1–N9. https://doi.org/10.1190/1.2159053

Biot MA (1941) General theory of three-dimensional consolidation. J Appl Phys 12(2):155–164. https://doi.org/10.1063/1.1712886

Blöcher G, Kluge C, Milsch H, Cacace M, Jacquey AB, Schmittbuhl J (2019) Permeability of matrix-fracture systems under mechanical loading–constraints from laboratory experiments and 3-D numerical modelling. Adv Geosci 49:95–104. https://doi.org/10.5194/adgeo-49-95-2019

Borgomano JV, Pimienta LX, Fortin J, Guéguen Y (2019) Seismic dispersion and attenuation in fluid-saturated carbonate rocks: effect of microstructure and pressure. J Geophys Res Solid Earth 124(12):12498–12522. https://doi.org/10.1029/2019JB018434

Borgomano JV, Gallagher A, Sun C, Fortin J (2020) An apparatus to measure elastic dispersion and attenuation using hydrostatic- and axial-stress oscillations under undrained conditions. Rev Sci Instrum 91(3):034502. https://doi.org/10.1063/1.5136329

Brajanovski M, Gurevich B, Schoenberg M (2005) A model for P-wave attenuation and dispersion in a porous medium permeated by aligned fractures. Geophys J Int 163(1):372–384. https://doi.org/10.1111/j.1365-246X.2005.02722.x

Cai JG, Zhao J (2000) Effects of multiple parallel fractures on apparent attenuation of stress waves in rock masses. Int J Rock Mech Min Sci 37(4):661–682. https://doi.org/10.1016/S1365-1609(00)00013-7

Carcione JM, Picotti S (2006) P-wave seismic attenuation by slow-wave diffusion: effects of inhomogeneous rock properties. Geophysics 71(3):O1–O8. https://doi.org/10.1190/1.2194512

Carcione JM, Santos JE, Picotti S (2012) Fracture-induced anisotropic attenuation. Rock Mech Rock Eng 45(5):929–942

Caspari E, Novikov M, Lisitsa V, Barbosa ND, Quintal B, Rubino JG, Holliger K (2019) Attenuation mechanisms in fractured fluid-saturated porous rocks: a numerical modelling study. Geophys Prospect 67(4-Rock Physics: from microstructure to seismic signatures):935–955. https://doi.org/10.1111/1365-2478.12667

Chapman M (2003) Frequency-dependent anisotropy due to mesoscale fractures in the presence of equant porosity. Geophys Prospect 51(5):369–379. https://doi.org/10.1046/j.1365-2478.2003.00384.x

Chapman S, Quintal B (2018) Numerical analysis of local strain measurements in fluid-saturated rock samples submitted to forced oscillations. Geophysics 83(5):MR309–MR316. https://doi.org/10.1190/geo2018-0071.1

Chapman S, Tisato N, Quintal B, Holliger K (2016) Seismic attenuation in partially saturated Berea sandstone submitted to a range of confining pressures. J Geophys Res Solid Earth 121(3):1664–1676. https://doi.org/10.1002/2015JB012575

Chapman S, Borgomano JV, Yin H, Fortin J, Quintal B (2019) Forced oscillation measurements of seismic wave attenuation and stiffness moduli dispersion in glycerine-saturated Berea sandstone. Geophys Prospect 67(4-Rock Physics: from microstructure to seismic signatures):956–968. https://doi.org/10.1111/1365-2478.12710

David EC, Fortin J, Schubnel A, Guéguen Y, Zimmerman RW (2013) Laboratory measurements of low-and high-frequency elastic moduli in Fontainebleau sandstone. Geophysics 78(5):D369–D379. https://doi.org/10.1190/geo2013-0070.1

Fleuchaus P, Blum P (2017) Damage event analysis of vertical ground source heat pump systems in Germany. Geotherm Energy 5(1):1–15. https://doi.org/10.1186/s40517-017-0067-y

Fortin J, Guéguen Y (2021) Porous and cracked rocks elasticity: macroscopic poroelasticity and effective media theory. Math Mech Solids 26(8):1158–1172. https://doi.org/10.1177/10812865211022034

Galvin RJ, Gurevich B (2009) Effective properties of a poroelastic medium containing a distribution of aligned cracks. J Geophys Res Solid Earth. https://doi.org/10.1029/2008JB006032

Galvin RJ, Gurevich B (2015) Frequency-dependent anisotropy of porous rocks with aligned fractures. Geophys Prospect 63(1):141–150

Gassmann F (1951) Elastic waves through a packing of spheres. Geophysics 16(4):673–685. https://doi.org/10.1190/1.1437718

Gudmundsson A, Løtveit IF (2014) Sills as fractured hydrocarbon reservoirs: examples and models. Geol Soc Lond Spec Publ 374(1):251–271. https://doi.org/10.1144/SP374.5

Guéguen Y, Boutéca M (eds) (2004) Mechanics of fluid-saturated rocks. Elsevier, Oxford

Guo J, Germán Rubino J, Barbosa ND, Glubokovskikh S, Gurevich B (2018a) Seismic dispersion and attenuation in saturated porous rocks with aligned fractures of finite thickness: theory and numerical simulations—part 1: P-wave perpendicular to the fracture plane. Geophysics 83(1):WA49–WA62. https://doi.org/10.1190/geo2017-0065.1

Guo J, Germán Rubino J, Barbosa ND, Glubokovskikh S, Gurevich B (2018b) Seismic dispersion and attenuation in saturated porous rocks with aligned fractures of finite thickness: theory and numerical simulations—Part 2: frequency-dependent anisotropy. Geophysics 83(1):WA63–WA71. https://doi.org/10.1190/geo2017-0066.1

Gurevich B, Brajanovski M, Galvin RJ, Müller TM, Toms-Stewart J (2009) P-wave dispersion and attenuation in fractured and porous reservoirs–poroelasticity approach. Geophys Prospect 57(2):225–237. https://doi.org/10.1111/j.1365-2478.2009.00785.x

Gurevich B, Makarynska D, de Paula OB, Pervukhina M (2010) A simple model for squirt-flow dispersion and attenuation in fluid-saturated granular rocks. Geophysics 75(6):N109–N120. https://doi.org/10.1190/1.3509782

Hunziker J, Favino M, Caspari E, Quintal B, Rubino JG, Krause R, Holliger K (2018) Seismic attenuation and stiffness modulus dispersion in porous rocks containing stochastic fracture networks. J Geophys Res Solid Earth 123(1):125–143

Li B, Jiang Y, Koyama T, Jing L, Tanabashi Y (2008) Experimental study of the hydro-mechanical behavior of rock joints using a parallel-plate model containing contact areas and artificial fractures. Int J Rock Mech Min Sci 45(3):362–375. https://doi.org/10.1016/j.ijrmms.2007.06.004

Lissa S, Barbosa ND, Caspari E, Alkhimenkov Y, Quintal B (2020) Squirt flow in cracks with rough walls. J Geophys Res Solid Earth 125(4):e2019JB019235. https://doi.org/10.1029/2019JB019235

Lubbe R, Sothcott J, Worthington MH, McCann C (2008) Laboratory estimates of normal and shear fracture compliance. Geophys Prospect 56(2):239–247. https://doi.org/10.1111/j.1365-2478.2007.00688.x

Matonti C, Guglielmi Y, Viseur S, Bruna PO, Borgomano J, Dahl C, Marié L (2015) Heterogeneities and diagenetic control on the spatial distribution of carbonate rocks acoustic properties at the outcrop scale. Tectonophysics 638:94–111. https://doi.org/10.1016/j.tecto.2014.10.020

Mazumder S, Karnik AA, Wolf KHA (2006) Swelling of coal in response to CO_2 sequestration for ECBM and its effect on fracture permeability. SPE J 11(03):390–398. https://doi.org/10.2118/97754-PA

Min KB, Lee J, Stephansson O (2013) Implications of thermally-induced fracture slip and permeability change on the long-term performance of a deep geological repository. Int J Rock Mech Min Sci 61:275–288. https://doi.org/10.1016/j.ijrmms.2013.03.009

Müller TM, Gurevich B, Lebedev M (2010) Seismic wave attenuation and dispersion resulting from wave-induced flow in porous rocks—a review. Geophysics 75(5):75A147-75A164. https://doi.org/10.1190/1.3463417

O'Connell RJ, Budiansky B (1977) Viscoelastic properties of fluid-saturated cracked solids. J Geophys Res 82(36):5719–5735. https://doi.org/10.1029/JB082i036p05719

O'Connell RJ, Budiansky B (1978) Measures of dissipation in viscoelastic media. Geophys Res Lett 5(1):5–8. https://doi.org/10.1029/GL005i001p00005

Paillet FL, Hess AE, Cheng CH, Hardin E (1987) Characterization of fracture permeability with high-resolution vertical flow measurements during borehole pumping. Groundwater 25(1):28–40. https://doi.org/10.1111/j.1745-6584.1987.tb02113.x

Pimienta L, Fortin J, Guéguen Y (2015) Bulk modulus dispersion and attenuation in sandstones. Geophysics 80(2):D111–D127. https://doi.org/10.1190/geo2014-0335.1

Pimienta L, Fortin J, Borgomano JV, Guéguen Y (2016) Dispersions and attenuations in a fully saturated sandstone: experimental evidence for fluid flows at different scales. Lead Edge 35(6):495–501. https://doi.org/10.1190/tle35060495.1

Quintal B, Steeb H, Frehner M, Schmalholz SM (2011) Quasi-static finite element modeling of seismic attenuation and dispersion due to wave-induced fluid flow in poroelastic media. J Geophys Res Solid Earth. https://doi.org/10.1029/2010JB007475

Quintal B, Jänicke R, Rubino JG, Steeb H, Holliger K (2014) Sensitivity of S-wave attenuation to the connectivity of fractures in fluid-saturated rocks. Geophysics 79(5):WB15–WB24. https://doi.org/10.1190/geo2013-0409.1

Rice JR, Cleary MP (1976) Some basic stress diffusion solutions for fluid-saturated elastic porous media with compressible constituents. Rev Geophys 14(2):227–241. https://doi.org/10.1029/RG014i002p00227

Spencer JW Jr, Shine J (2016) Seismic wave attenuation and modulus dispersion in sandstones. Geophysics 81(3):D211–D231. https://doi.org/10.1190/geo2015-0342.1

Ulven OI, Storheim H, Austrheim H, Malthe-Sørenssen A (2014) Fracture initiation during volume increasing reactions in rocks and applications for CO_2 sequestration. Earth Planet Sci Lett 389:132–142. https://doi.org/10.1016/j.epsl.2013.12.039

Vinci C, Renner J, Steeb H (2014) On attenuation of seismic waves associated with flow in fractures. Geophys Res Lett 41(21):7515–7523. https://doi.org/10.1002/2014GL061634

White JE (1975) Computed seismic speeds and attenuation in rocks with partial gas saturation. Geophysics 40(2):224–232. https://doi.org/10.1190/1.1440520

Zimmerman RW (2000) Coupling in poroelasticity and thermoelasticity. Int J Rock Mech Min Sci 37(1–2):79–87. https://doi.org/10.1016/S1365-1609(99)00094-5

Biot MA, Willis DG (1957) The elastic coefficients of the theory of consolidationhttps://doi.org/10.1115/1.4011606

Borgomano J (2018) Dispersion des modules élastiques de carbonates saturés: étude expérimentale et modélisation. Doctoral dissertation, Université Paris sciences et lettres

Goodman RE (1976) Methods of geological engineering in discontinuities of rocks: west, St. Paul, Minn

Kluge C, Blöcher G, Milsch H, Hofmann H, Nicolas A, Li Z, Fortin J (2017) Sustainability of fractured rock permeability under varying pressure. In: Poromechanics VI, pp 1192–1199. https://doi.org/10.1061/9780784480779.148

Nakagawa S (2013) Low-frequency (< 100 Hz) dynamic fracture compliance measurement in the laboratory. In: 47th US Rock Mechanics/Geomechanics Symposium. American Rock Mechanics Association

Walsh JB (1981) Effect of pore pressure and confining pressure on fracture permeability. In: International journal of rock mechanics and mining sciences & geomechanics abstracts, vol 18(5). Pergamon, pp 429–435. https://doi.org/10.1016/0148-9062(81)90006-1

Winkler KW, Murphy III WF (1995) Acoustic velocity and attenuation in porous rocks. Rock physics and phase relations. A Handbook of physical constants, pp 20–34. https://doi.org/10.1029/RF003